nature communications

Article

https://doi.org/10.1038/s41467-025-67035-6

Anti-swelling and self-activating artificial proteoglycan assemblies as cartilaginous implant for post-microfracture healing

Received: 31 March 2025

Accepted: 20 November 2025

Published online: 06 December 2025

Check for updates

Zhulian Li[1,2,6], Mingda Zhao[1,2,6], Jiayi Zhu[1,2,6], Yuxiang Wang[1,2], Xiaolin Xiao[1,2], Zhaoxi Deng[3], Xu Peng[3], Junli Liu[4], Jie Liang[1,2,5], Qing Jiang[1,2], Yujiang Fan[1,2], Xingdong Zhang[1,2] & Yong Sun[1,2]

The poor structural stability and insufficient endogenous activation of cartilaginous implant might be key factors for cartilage regeneration after microfracture. Herein, inspired by the restrictive effect of collagen fibers on proteoglycans, we develop artificial proteoglycan assemblies (DSPG@Pep) through sequential co-assembly of bioactive polysaccharide, protein and peptides via electrostatic interactions and covalent conjugation. The DSPG@Pep presents anti-swelling, compression and degradation resistance properties, and significantly activates endogenous stem cell recruitment and direct chondrogenic differentiation. Specifically, the DSPG@Pep downregulates the calcium signaling pathway (e.g., *CACNA1G*, *AVPR1A*, et al.) and ECM-receptor interaction (*IBSP* and *COL4A2*), thus reduces ossification (*EFEMP1*, *SCUBE3*, and *SPARCL1*) tendency as evidenced by decreased cytosolic calcium concentration and integrin β1 clustering. Cartilage defects models in male rabbits and pigs confirm the DSPG@Pep can be stably immobilized in the defect sites and facilitate the structural and functional remodeling of neocartilage. These findings provide a promising biomaterial design strategy for endogenous cartilage regeneration.

Microfracture surgery (MF), which activates endogenous cells to promote the repair of cartilage defects, has been extensively used in clinical practices[1]. However, the subsequent regenerated fibrocartilage tissue demonstrates poor mechanical properties and is prone to postoperative degeneration and ossification[2,3]. The poor structural stability and insufficient endogenous activation of implanted biomaterials might be key factors for effective cartilage regeneration after microfracture surgery. In natural cartilage matrices, the collagen fiber network synergizes with proteoglycan aggregates (PG) to provide cartilage tissue with dual rheological properties and tribological properties[4]. Studies have confirmed that the failure or damage of the collagen assembly leads to proteoglycan swelling, increased tissue hydration, matrix softening, and eventual degeneration[5]. Therefore, the restrictive effect of collagen fibers on PGs is vital for maintaining structural stability of cartilage. These microstructural insights demonstrate that proteins play pivotal roles in the formation of the cartilage matrix architecture, the maintenance of its anti-swelling, compression and degeneration resistance, as well as biological regulatory functions.

However, the mechanisms by proteins in native cartilage stabilizing PG structures and biofunction have not been effectively utilized in developing high-quality biomimetic cartilage matrix. Specifically, in

[1]National Engineering Research Center for Biomaterials, Sichuan University, 29# Wangjiang Road, Chengdu, Sichuan, China. [2]College of Biomedical Engineering, Sichuan University, 29# Wangjiang Road, Chengdu, Sichuan, China. [3]West China School of Basic Medical Sciences & Forensic Medicine, Experimental and Research Animal Institute, Sichuan University, Chuanda Road, Chengdu, China. [4]Department of Orthopedics, Chongqing General Hospital, 118 Xingguang Avenue, Liangjiang New District, Chongqing, China. [5]Sichuan Testing Center for Biomaterials and Medical Devices, Sichuan University, 29# Wangjiang Road, Chengdu, China. [6]These authors contributed equally: Zhulian Li, Mingda Zhao, Jiayi Zhu. e-mail: sunyong8702@scu.edu.cn

native cartilage, the core protein of proteoglycans interacts with hyaluronan (HA) to collectively stabilize the PG network, while the rigid collagen fiber network limits excessive swelling of the PG, which derived from the hydration of anionic HA[6,7]. Therefore, how to simulate the proteins to limit the structural instability caused by the hydration of HA, and maintain its lubrication and biofunctions is of great importance. Among various natural proteins, silk fibroin (SF) with alternating sequence of hydrophilic and hydrophobic amino acids has been widely used for fabricating biomimetic cartilage matrix[8,9]. The amino acid residues in its light chain are conducive to chemical modification to provide cross-linking sites to restrict the movement of hydrophilic polysaccharide molecular chains[10]. While the heavy chain can trigger the β-sheet nanocrystal formation by hydrophobic assembly among SF molecules to stable structural network and improve mechanical strength[11–13]. Hence, we hypothesized that integrating HA into the self-assembly structure of SF might be a potential strategy for constructing artificial proteoglycan assemblies.

Additionally, the rich proteoglycan mediates the interactions of chondrocytes with growth factors, cytokines and extracellular matrix components, which regulate signal transduction and control the adhesion, proliferation, differentiation and metabolic activities of chondrocyte[14,15]. However, the single structural regulation of biomimetic cartilage matrix is difficult to efficiently activate endogenous regeneration. The introduction of cells, growth factors, small-molecule drugs and peptides can compensate the intrinsic limitations on insufficient biofunctions of biomimetic cartilage matrix[16–20]. Therein, the peptides with specific design as bioactive materials could bind to or mimic the in vitro functional growth factor or proteins to participate receptor activation, factor recruitment or biological signal transduction for enhancing tissue regeneration[21,22]. For instance, VEGF-mimetic multidomain peptide activates VEGFR1, VEGFR2, and NP-1 receptors to enhance angiogenesis[23]. RGD peptides derived from fibronectin increase the integrin-mediated extracellular vesicles loading in supramolecular hydrogel to improve renal repair[24]. TGF-β1-affinity peptide enhanced endogenous TGF-β1 enrichment and stem cells recruitment to promote cartilage regeneration[25]. Therefore, functional peptides-mediated artificial proteoglycan assemblies might efficiently promote endogenous activation.

Here, we construct artificial proteoglycan assemblies by the molecular-level co-assembly. Briefly, thiolated-HA (HASH) was preliminarily assembled with polyphenol-modified SF (SFD) to form the precursor of DSPG (SFDHS) with irregular stretching deformations by electrostatic interaction, and then chemically assembling drove SFDHS to transform into fiber bundles (DSPG). Subsequently, the thiolated-peptide (Pep-SH) was integrated into DSPG to form artificial proteoglycan assemblies (DSPG@Pep) with structural stability and endogenous activation (Fig. 1a, b). The in vitro cell experiments and transcriptomic analyses reveal that DSPG@Pep promotes the chondrogenic differentiation of bone marrow mesenchymal stem cells (BMSCs) by downregulating the calcium signaling pathway and ECM-receptor interaction, and thus reduces the trend of ossification as evidenced by the decreased cytosolic calcium concentration and integrin β1 clustering. The rabbit and pig articular cartilage regeneration models confirm the safety and efficacy of the anti-swelling and self-activating artificial proteoglycan assemblies (Fig. 1c). This strategy provides a potential biomaterial design pathway for clinical MF treatment.

Results

Constructing DSPG by molecular-level co-assembly strategy

Here, we constructed artificial proteoglycan assemblies via electrostatic interactions and chemical driven co-assembly of SFD and HASH. And the structure displayed distinct change during the assembly process (Fig. 2a). First, HASH and SFD were synthesized via amidation reaction (Supplementary Fig. 1a and 1b). The proton nuclear magnetic resonance (^{1}H NMR) spectrum of HASH (Supplementary Fig. 1c) exhibited a methylene proton peak at 2.8 ppm, which indicated the successful grafting. And the sulfhydryl grafting efficiency was approximately 20%. Fourier transform infrared (FT-IR) spectroscopy (Supplementary Fig. 1d) confirmed the successful grafting of dopamine onto SF, as evidenced by a characteristic peak at 1555 cm^{-1}, corresponding to aromatic C = C stretching vibrations or amide II band N-H bending. Then, we mixed SFD and HASH at a ratio of 1:2, and adjusted the pH to 7 to construct the DSPG. The transmission electron microscopy (TEM) and atomic force microscopy (AFM) were employed to observe the orderly structural changes during the assembly process. These results demonstrated that both SF and SFD formed spherical micelles in aqueous solution (Fig. 2b, c and Supplementary Fig. 2a, b). After mixing with HASH, the SFHS (as precursor of SPG) formed spherical aggregates with diameters of 20-100 nm (Supplementary Fig. 2a and b), while the SFDHS (as precursor of DSPG) displayed irregular stretching deformations and locally directional fiber bundles formation at the edges (Fig. 2b, c). Further adjusting pH to 7, chemical assembly enabled DSPG to form fiber bundles (Fig. 2b, c), whereas SPG remained as spherical micelles (Supplementary Fig. 2a and b). Phalloidin staining and confocal laser scanning microscopy (CLSM) observing confirmed that SF remained as spherical micelles within the SPG hydrogel, while SFD promoted the formation of co-assembly network in DSPG (Supplementary Fig. 2c).

Furthermore, the structure changes during assembly process were further explored from intermolecular interactions. Firstly, the solution of SFHS (as precursor of SPG) remained transparent in the mixed state, whereas that of SFDHS (as precursor of DSPG) appeared as a milky suspension (Supplementary Fig. 2d), which might be attributed to electrostatic interactions between SFD and HASH. The ζ-potential measurements (Fig. 2d) indicated SF and HASH were negatively charged, whereas SFD was positively charged, which confirmed the above speculation. The isothermal titration calorimetry (ITC) results illustrated that the assembly processes of DSPG and SPG presented exothermic reactions, and the heat change tended to stabilize after the first injection (pH 7), implying the formation of chemical bonds (Supplementary Fig. 3a and b). These results revealed that the electrostatic interactions and chemical driven co-assembly might be the primary reasons for structural changes.

As is known to all, the microstructure and functions of SF are closely related to its secondary structure. The secondary structures of silk fibroin include β-Sheet, random coil, α-helix and β-turn. The β-Sheet dominates high strength, slow degradation and hydrophobic properties, while random coil and α-helix dominate flexibility, fast degradation and hydrophilicity. The effective increase in β-sheet content is conducive to enhancing mechanical strength, slowing down the degradation rate, and resisting swelling behavior[8,10,13,26]. Therefore, we further utilized Thioflavin T (ThT) to determine the changes of β-sheet content at each assembly stage of SPG and DSPG over time. The assembly processes of SPG and DSPG at pH 7 seemed instant (Supplementary Fig. 3c and e). The β-sheet content decreased when mixed SF and HASH, even at pH 7 (Supplementary Fig. 3d). This might be due to the electrostatic repulsion between SF and HASH, as well as the formation of disulfide bonds among HASH, which caused the SF molecular chains unfolding to hinder β-sheet formation. On the contrary, the β-sheet content in DSPG was 3.5 times of the original SFD, which hardly changed over time (Supplementary Fig. 3e and f). This might be due to the chemical reaction occurred between SFD and HASH at pH 7, which drove the rapid assembly. In addition, the final β-sheet content of DSPG was much higher than that of SPG (Fig. 2e). Circular dichroism (CD) spectroscopy and quantitative analysis (Fig. 2f) further confirmed the higher content of β-sheet in DSPG. The micromechanical properties using nanoindentation verified that the effective Young's modulus of DSPG was approximately 5.8 MPa (3 times that of SPG) (Fig. 2g), which should be attributed to the efficacy of β-sheet.

https://doi.org/10.1038/s41467-025-67035-6

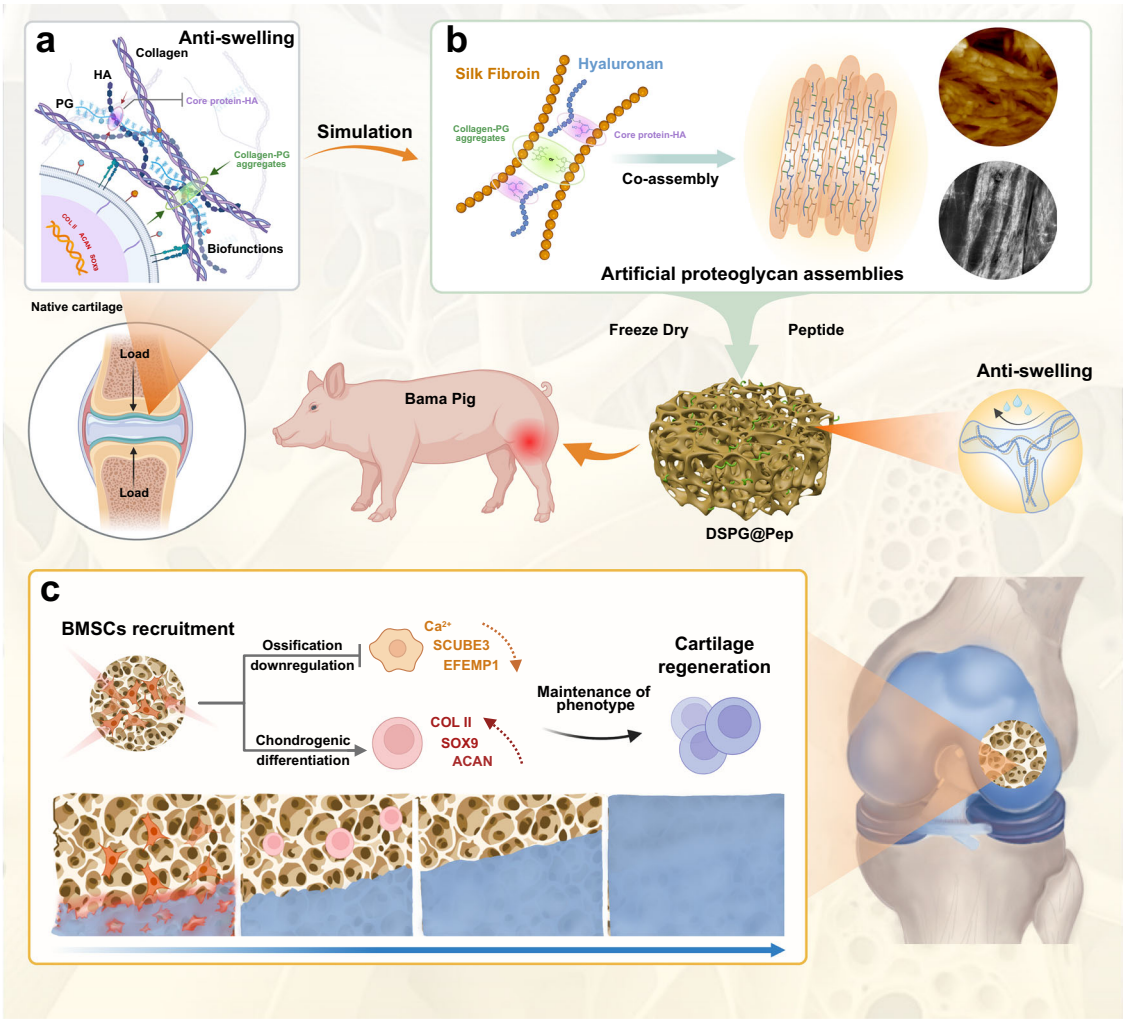

Fig. 1 | Anti-swelling and self-activating artificial proteoglycan assemblies simulating the core-HA-collagen interactions and biofunctions of native cartilage matrix and how this promotes cartilage regeneration. a Illustration of the interactions and biofunctions in native articular cartilage. The core protein of PG interacts with hyaluronan to stabilize the PG aggregates network (indicated by purple circle), while the rigid collagen fibers restrict its swelling behavior (indicated by green circle). The interactions between matrix and chondrocytes mediate the adhesion, proliferation, differentiation and metabolism. **b** DSPG@Pep was fabricated by molecular-level co-assembly to simulate the interactions and biofunctions. **c** In vitro and in vivo experiments revealed that DSPG@Pep significantly promote endogenous cartilage regeneration by BMSCs recruitment and chondrogenic differentiation through downregulating calcium signaling pathway and ossification. Created in BioRender. Dong, H. (https://BioRender.com/1k38mex).

The structural stability of DSPG

In order to further realize the application in the cartilage defects, the hydrogels were freeze-dried to prepare the sponge-like scaffolds (Fig. 2h), and its structural stability including anti-swelling, compression and degradation resistance was tested. The swelling test results showed that SPG swelled rapidly in PBS solution, and its diameter doubled soon. However, DSPG exhibited almost no change in shape after 30 h and a significantly lower water absorption capacity upon reaching the swelling equilibrium compared to SPG (Fig. 2i). The compressive stress–strain curves indicated that DSPG achieved a stress value of approximately 37.5 kPa at 75% strain (Supplementary Fig. 4a and Fig. 2j), 3 times that of SPG. Cyclic compressive curve further identified the compression resistance of DSPG (Fig. 2k). These results confirmed the effectiveness of co-assembly in promoting anti-swelling property and enhancing compression resistance. The FT-IR spectra (Supplementary Fig. 4b) revealed that there were significant differences between SPG and DSPG in the peak positions of amide I and II bands (1500–1700 cm^{-1}). And fourier self-deconvolution (FSD) analysis indicated a higher content of β-sheet conformations in DSPG compared to SPG (Fig. 2 l1–l4). The thioflavin T fluorescence staining images (Supplementary Fig. 4c) also confirmed the higher content of β-sheet in DSPG. These results suggested that the conformation changes caused by co-assembly might be the fundamental reason for the enhanced anti-swelling and mechanical properties. To identify the optimal artificial proteoglycan assemblies, we prepared DSPG in various ratios including DSPG (1: 4), DSPG (1: 2), DSPG (1: 1), DSPG (2: 1) and DSPG (4: 1). The swelling, degradation, pore structure, shape stability, and mechanical characteristics were evaluated (Supplementary Fig. 5a–i). The screening procedure manifested that DSPG (1: 2) was the most suitable, which was named as DSPG and used in subsequent experiments (Fig. 2m).

DSPG conjugated with bioactive peptides promote the self-activating biofunctions

To enhance the self-activating biofunctions, we conjugated functional peptides onto the surface of DSPG, and implemented two in vitro experiments (Transwell model with pore size 8 μm and cell scratch assay) to evaluate BMSCs recruitment (Fig. 3a). First, FT-IR spectroscopy (Supplementary Fig. 6a) and X-ray photoelectron spectroscopy (XPS) (Supplementary Fig. 6b) confirmed the successful grafting of the

https://doi.org/10.1038/s41467-025-67035-6

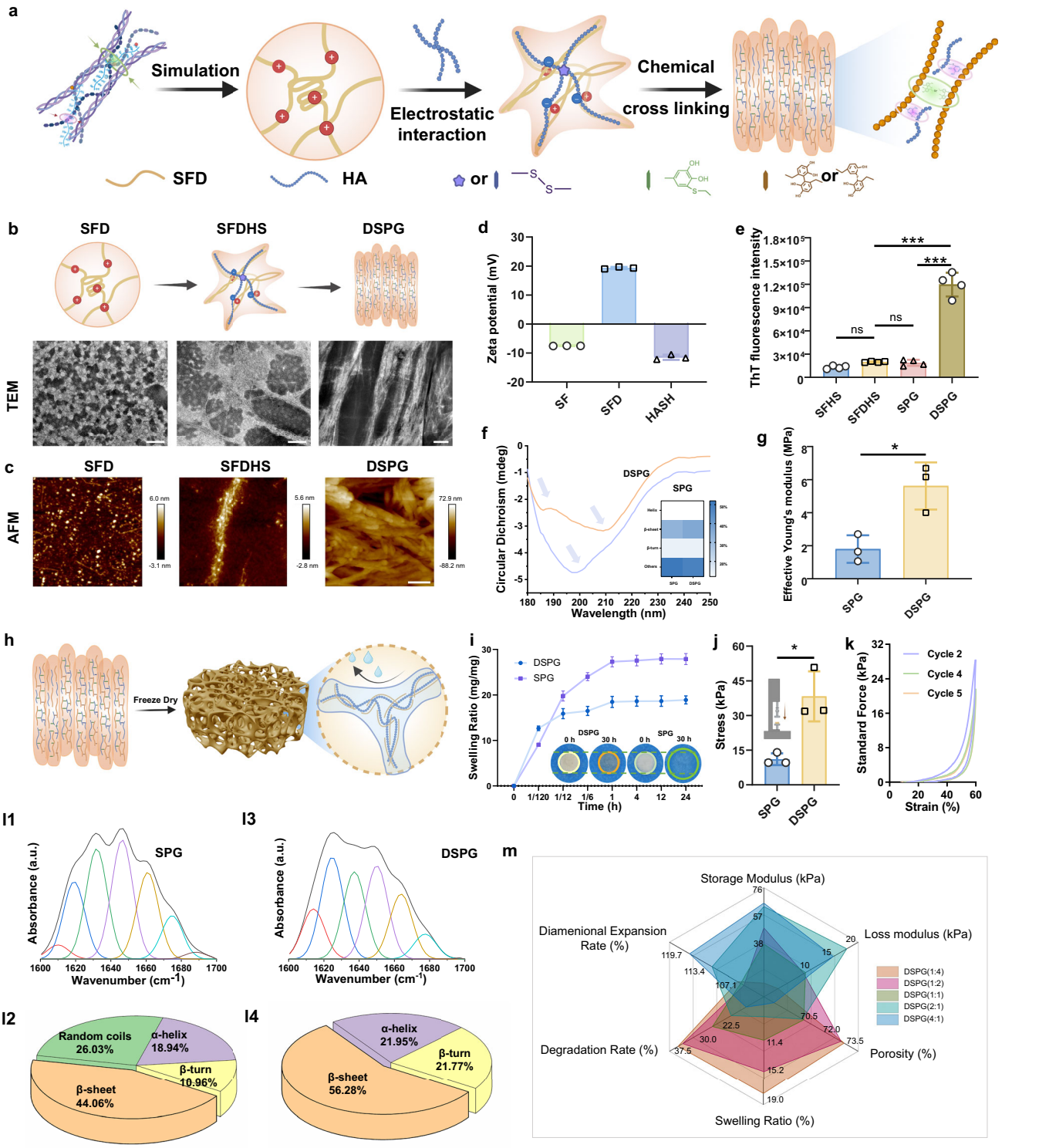

functional peptides (DSPG@Pep). Scanning electron microscopy (SEM) images, porosity and pore size analyses indicated that the microstructure was largely unchanged after peptides conjugation (Supplementary Fig. 6c–e), resulting in no effect on the mass transfer and mechanical properties (Supplementary Fig. 6f–i). The cumulative release curve indicated that 20% of peptide was released in the first 10 days, and then the cumulative release volume reached a plateau (Supplementary Fig. 6j). This suggested that the released peptide (20%) might promote cell recruitment into the scaffold in the initial stage, and then the residual peptide (80%) modified on the scaffold could regulate the chondrogenic differentiation of recruited endogenous BMSCs. The results of fluorescein diacetate/propidium iodide (FDA/PI) staining and CCK-8 kit assay showed that both DSPG and DSPG@Pep effectively promoted BMSCs proliferation (Supplementary Fig. 6k and l). Furthermore, cytoskeleton staining revealed that BMSCs were spreading on the surface of DSPG@Pep, with significant differences in the spreading area compared to SPG (Supplementary Fig. 6m and n).

In addition, one week after in vivo implantation, SPG presented obvious swelling, while the volume of DSPG and DSPG@Pep remained

Fig. 2 | Constructing DSPG by molecular-level co-assembly strategy. **a** Schematic of the bioinspired design and assembly process. Green circle, the chemical bond between SFD. Purple circle, the chemical bond between SFD and HASH. Created in BioRender. Dong, H. (https://BioRender.com/1sendhs). **b** Microstructure changes of SFD, SFDHS and DSPG observed by TEM. Scale bar, 100 nm (SFD and SFDHS); 500 nm (DSPG). Created in BioRender. Dong, H. (https://BioRender.com/tqwo99r). **c** AFM images of SFD, SFDHS and DSPG. Scale bar, 200 nm. **d** ζ-potential of SF, SFD, and HASH. Error bars represent standard deviation. $n = 3$ independent replicates. **e** Thioflavin T staining fluorescence intensity during assembly. Error bars represent standard deviation. $n = 4$ independent replicates. ($^{ns}p = 0.639$, $^{ns}p = 0.998$, $^{***}p = 3.41 \times 10^{-10}$, $^{***}p = 3.05 \times 10^{-10}$). **f** CD spectrum and secondary structure analysis. **g** Effective Young's Modulus measured by nanoindentation. Error bars represent standard deviation. $n = 3$ independent replicates. ($^{*}p = 0.016$). **h** Schematic of the lyophilization process for fabricating sponge-like DSPG. Created in BioRender. Dong, H. (https://BioRender.com/57mxl3c). **i** Swelling ratio and dimensional changes of sponge-like SPG and DSPG. Error bars represent standard deviation, n = 3 independent replicates. **j** Stress values of SPG and DSPG at 75% strain. Error bars represent standard deviation. $n = 3$ independent replicates. ($^{*}p = 0.014$). **k** Cyclic compression curve of DSPG. **l1–l4** Fourier self-deconvolution (FSD) analysis of protein secondary structures in SPG and DSPG, with pie charts illustrating the proportions of different secondary structures. **m** Radar chart evaluating storage modulus, loss modulus, porosity, swelling ratio, degradation rate, and deformation ratio of DSPGs with varying SFD/HASH ratios. Statistical analyses were performed with one-way ANOVA, followed by Tukey's multiple comparison post hoc test, $^{*}p < 0.05$, $^{**}p < 0.01$ and $^{***}p < 0.001$. Source data are provided as a Source Data file.

basically stable. The mass of all groups was improved, which might be tissue fluid infiltration and cells ingrowth. At 5 and 9 weeks, the mass of all the groups was higher than initial mass, but the volume change rate of SPG was the maximum (Supplementary Fig. 7a–c), which indicated that SPG had undergone significant degradation, while the other two groups was slower. These further confirmed that the assembly strategy enhanced anti-swelling and degradation resistance.

Results of transwell model and cell scratch assay in vitro (Fig. 3b–e) indicated that both DSPG and DSPG@Pep possess the capabilities in promoting the lateral and longitudinal migration of BMSCs, especially DSPG@Pep. Additionally, we conducted an in situ endogenous stem cell recruitment experiment using a rabbit articular cartilage defect model (Fig. 3f). The immunofluorescence (IF) staining results (Fig. 3g and Supplementary Fig. 8a) of typical stem cell surface markers (CD73, CD44, CD90) showed that both DSPG and DSPG@Pep could promote the endogenous stem cells recruitment. Especially, DSPG@Pep exhibited an enhanced recruitment effect, which could provide a rich source of stem cells for cartilage regeneration in situ.

To investigate the ability of promoting BMSCs chondrogenic differentiation, an in vitro co-culture model was constructed. After 21 days of co-culture under chondrogenic induced conditions, safranin-O (SO) (Fig. 3h) and IF staining images (Fig. 3i) suggested that although DSPG could promote the secretion of glycosaminoglycans (GAGs) and collagen type II (*COL II*), it also increased the secretion of collagen type X (*COL X*). However, DSPG@Pep significantly increased the secretion of GAGs and COL II while reducing that of *COL X*. Significant differences in the GAG/DNA ratios (Supplementary Fig. 8b, c and Fig. 3j) further confirmed the role of DSPG@Pep in improving chondrogenic differentiation. Furthermore, RT-qPCR analysis indicated higher relative expression levels of *ACAN*, *SOX9*, and *COL II* (Fig. 3k–m), along with lower relative expression levels of *COL I* and *COL X* (Fig. 3n, o). These results demonstrated the potential of DSPG@Pep to promote BMSCs chondrogenic differentiation while inhibiting fibrosis and hypertrophy.

Transcriptomic analysis to reveal the mechanism of DSPG@Pep regulating stem cells chondrogenic differentiation

As shown in Fig. 4a, transcriptomic analysis was employed to investigate how DAPG@pep regulate the fate of BMSCs during chondrogenic differentiation. The Pearson correlation between samples indicates good biological repetition (Supplementary Fig. 9a and b). Volcano plots reveal that 477 genes were significantly upregulated and 259 genes downregulated in DSPG compared with SPG (Supplementary Fig. 9c), while 115 genes significantly upregulated and 380 genes downregulated in DSPG@Pep compared to DSPG (Supplementary Fig. 9d). Among these, differentially expressed genes were analyzed using Gene Ontology (GO) and the Kyoto Encyclopedia of Genes and Genomes (KEGG) database. The database analysis of upregulated pathways (Fig. 4b1) indicated that DSPG enhanced cell adhesion and proliferation (Focal adhesion, ECM–receptor interactions, and Cell cycle), and significantly activated calcium signaling pathways compared to SPG. According to the GO analysis (Fig. 4c1), the upregulated genes in DSPG are enriched in ossification, bone mineralization, calcium ion binding, and voltage-gated cation channel activity compared to SPG. A comparative KEGG analysis of downregulated pathways in DSPG@Pep and DSPG (Fig. 4b2) demonstrated that DSPG@Pep markedly suppressed the calcium signaling pathway. The corresponding GO analysis of DSPG@Pep and DSPG (Fig. 4c2) indicated that the downregulated genes are enriched in ossification, bone mineralization, calcium ion binding, and voltage-gated cation channel activity. The specific gene–pathway interaction diagram and relative gene expression in selected pathways are displayed in Fig. 4d. The calcium signaling pathway is involved in multiple differentially expressed genes, including *CACNA1G*, *AVPR1A*, *PLCB1*, *RET*, *MST1R*, and *RYR3*. A specific gene heatmap (Fig. 4e) elucidated the relevant up- or downregulated genes in the GO and KEGG analyses of DSPG vs. SPG and DSPG@Pep vs. DSPG. In total, the transcriptomic analysis indicated that DSPG could promote BMSC adhesion and proliferation (ECM–receptor interactions, cell cycle), while upregulating the calcium signaling pathway and ossification. In contrast, DSPG@Pep downregulated the calcium signaling pathway (e.g., *CACNA1G*, *AVPR1A* et al.), ossification and bone mineralization (*EFEMP1*, *SCUBE3*, and *SPARCL1*).

To validate the transcriptomic results, we assessed the expression levels of related genes in calcium signaling pathway and ossification, as well as cytoplasmic calcium concentration. The RT-qPCR results (Supplementary Fig. 9e–h and Fig. 4f1–f5) and calcium fluorescence imaging (Fig. 4g) confirmed that DSPG promoted the expression of genes regulating the influx of extracellular calcium ions (*CACNA1G*), the release of intracellular calcium ions (*AVPR1A, PLCB1, RET, MST1R, and RYR3*), as well as ossification (*EFEMP1*, *SCUBE3*, and *SPARCL1*), resulting in increase of cytoplasmic calcium concentration. Conversely, DSPG@Pep maintained lower cytoplasmic calcium concentration by downregulating the related gene expression, thereby suppressing ossification genes. Overall, the transcriptomic analysis and verifications demonstrated that DSPG@Pep could downregulate the calcium signaling pathway and ossification, which might be beneficial for chondrogenic differentiation and phenotype maintenance (Fig. 4h).

Studies have shown that the interaction between cells and ECM is mainly mediated by integrins, while the interaction among cells is mediated by N-cadherin[27]. Integrins and N-cadherin competitively regulate cofilin phosphorylation, thereby adjusting the mechanical sensing of human marrow stem cells (hMSCs). The N-cadherin ligation can inhibit the mechanical sensing sensitivity induced by integrin ligation, thereby suppressing osteogenic differentiation of hMSCs[28]. Notably, the ECM-receptor interaction pathway displayed significant differences when DSPG vs. DSPG@Pep and DSPG@Pep vs. DSPG (Fig. 4b1, b2). So, the differential genes were assessed by RT-qPCR, including integrin-binding sialoprotein (*IBSP*), collagen type IV alpha2 (*COL4A2*) and tenascin-C (*TNC*), which can combine with integrins to promote ossification, vascularization and fibrosis respectively[29–32].

https://doi.org/10.1038/s41467-025-67035-6

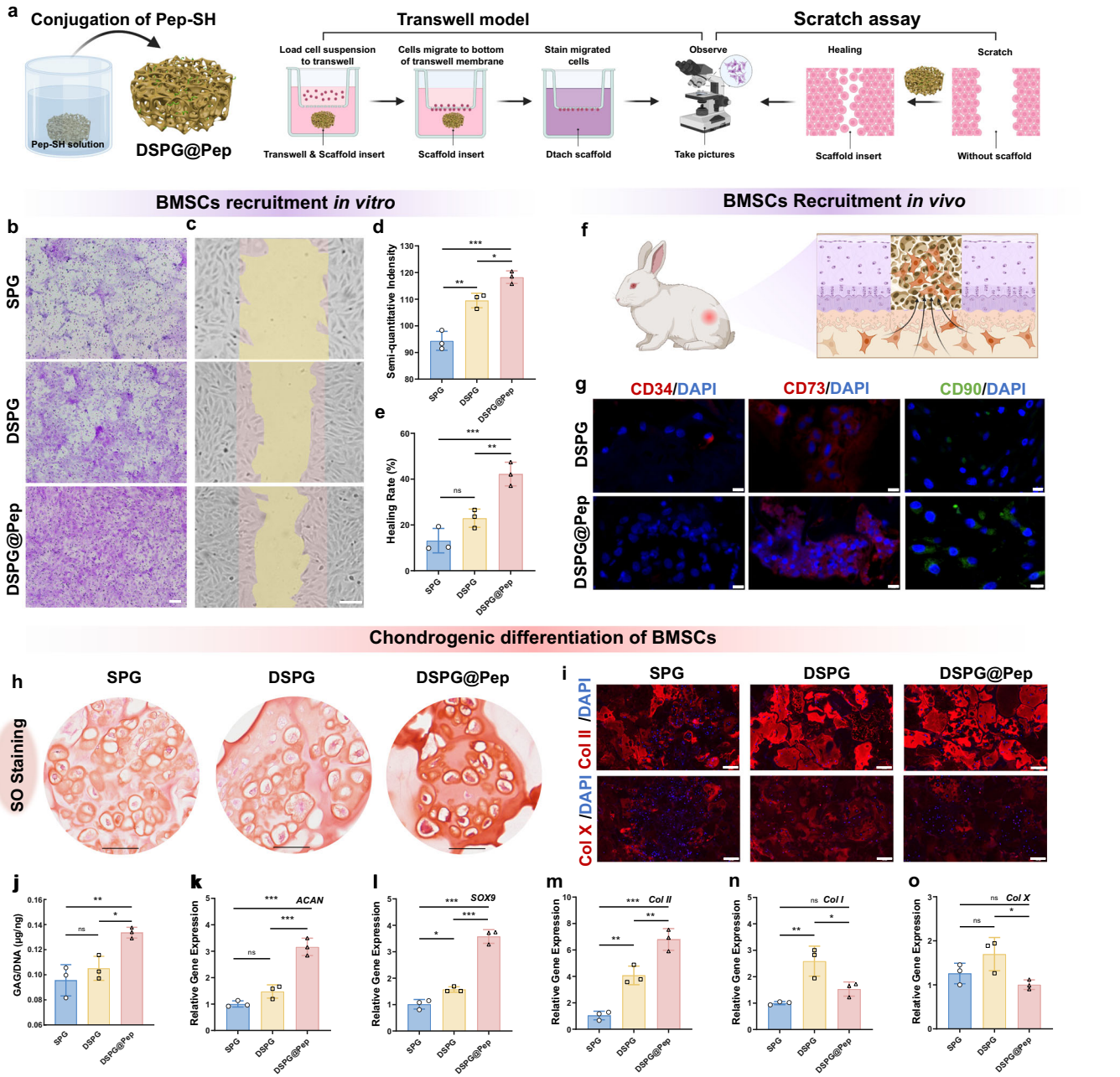

Fig. 3 | DSPG conjugated with bioactive peptides promote the self-activating biofunctions. a Schematic of DAPG@Pep preparation and stem cell recruitment in vitro. Created in BioRender. Dong, H. (https://BioRender.com/i2bcxxc). **b** Transwell model and crystal violet staining to assess the vertical BMSCs migration. Scale bar, 50 μm. **c** Scratch assay evaluates the horizontal BMSCs migration. Scale bar, 100 μm. **d** Semi-quantitative analysis of migrated cells via absorbance measurements after acetic acid elution of crystal violet-stained samples. Error bars represent standard deviation, $n = 3$ independent replicates. ($^{*}p = 0.024$, $^{**}p = 1.74 \times 10^{-3}$, $^{***}p = 1.41 \times 10^{-4}$). **e** Quantification of scratch wound healing rate to assess horizontal migration. Error bars represent standard deviation, $n = 3$ independent replicates. ($^{ns}p = 0.107$, $^{**}p = 6.80 \times 10^{-3}$, $^{***}p = 8.14 \times 10^{-4}$). **f** Schematic of endogenous stem cell recruitment in vivo. Created in BioRender. Dong, H. (https://BioRender.com/8ifbbex). **g** IF staining of CD34, CD73, CD90 and DAPI after 7 days post-implantation. Scale bar, 10 μm. **h** SO staining after 21 days of chondrogenic induction in vitro. Scale bar, 50 μm. **i** IF staining of Col II and Col X. Scale bar, 100 μm. **j** GAG/DNA quantitative analysis. Error bars represent standard deviation, $n = 3$ independent replicates. ($^{*}p = 0.0234$, $^{**}p = 0.0062$). **k**–**o** RT-qPCR analysis of *Acan*, *Sox9*, *Col II*, *Col I*, and *Col X*. Error bars represent standard deviation, $n = 3$ independent replicates. ($^{ns}p = 0.127$, $^{***}p = 9.89 \times 10^{-5}$, $^{***}p = 3.97 \times 10^{-4}$; $^{*}p = 0.027$, $^{***}p = 7.68 \times 10^{-6}$, $^{***}p = 3.42 \times 10^{-5}$; $^{**}p = 0.003$, $^{**}p = 0.0053$, $^{***}p = 9.14 \times 10^{-5}$; $^{ns}p = 0.252$, $^{*}p = 0.0281$, $^{**}p = 0.0043$; $^{ns}p = 0.183$, $^{ns}p = 0.506$, $^{*}p = 0.0415$). Statistical analyses were performed with one-way ANOVA, followed by Tukey's multiple comparison post hoc test, $^{*}p < 0.05$, $^{**}p < 0.01$ and $^{***}p < 0.001$. Source data are provided as a Source Data file.

These results illustrated that DSPG significantly increased the expression of *COL4A2* and *IBSP* in comparison with SPG, while DSPG@Pep significantly decreased the expression of *IBSP* in comparison with DSPG (Fig. 4i, j), and there was no significant difference in *TNC* (Supplementary Fig. 9i), indicating that DSPG might promote ossification and vascularization through interaction with integrin receptors, while DSPG@Pep was conducive to chondrogenic differentiation by weaking the ossification tendency. Further immunofluorescence staining revealed that DSPG promoted the integrin β1 clustering, but DSPG@Pep declined the integrin β1 and improved the N-cadherin clustering (Fig. 4k). These results further indicated that DSPG synchronously enhanced chondrogenic differentiation and cell

https://doi.org/10.1038/s41467-025-67035-6

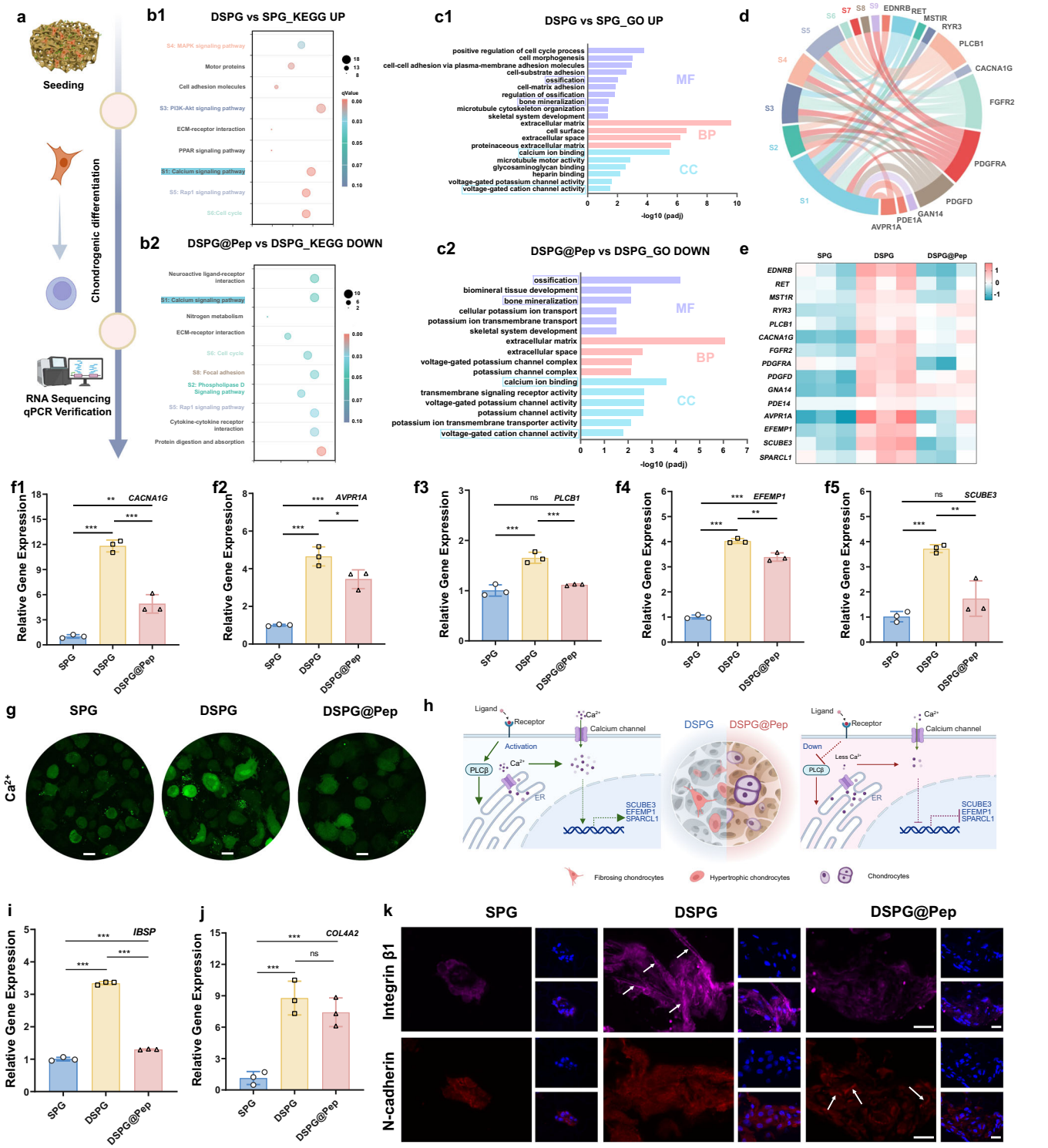

Fig. 4 | Transcriptomic analysis to reveal the mechanism of DSPG@Pep regulating the BMSCs chondrogenic differentiation. a Procedure of transcriptome and verification to evaluate the BMSCs chondrogenic differentiation on materials. Created in BioRender. Dong, H. (https://BioRender.com/pxnf8vy). **b1** Up-regulated terms in enriched KEGG analysis of DSPG vs. SPG. **b2** Down-regulated terms in enriched KEGG analysis of DSPG@Pep vs. DSPG. **c1**, Up regulated terms in enriched GO analysis of DSPG vs. SPG. **c2** Down-regulated terms in enriched GO analysis of DSPG@Pep vs. DSPG. **d**, Circular visualization of pathway-gene enrichment analysis. **e** Heatmap of gene regulation in specific pathways. **f1-f5**, RT-qPCR validation for representative genes. Error bars represent standard deviation, $n = 3$ independent replicates. ($^{**}p = 1.95 \times 10^{-3}$, $^{***}p = 5.48 \times 10^{-6}$, $^{***}p = 7.94 \times 10^{-5}$; $^{*}p = 0.026$, $^{***}p = 8.50 \times 10^{-4}$, $^{***}p = 8.87 \times 10^{-5}$; $^{ns}p = 0.347$, $^{***}p = 3.08 \times 10^{-4}$, $^{***}p = 8.84 \times 10^{-4}$; $^{**}p = 1.43 \times 10^{-3}$, $^{***}p = 8.96 \times 10^{-7}$, $^{***}p = 2.99 \times 10^{-7}$; $^{ns}p = 0.184$, $^{**}p = 3.33 \times 10^{-3}$, $^{***}p = 6.43 \times 10^{-4}$). **g**, CLSM images of calcium ion by fluorescence probe staining. Scale bar, 20 μm. **h**, Schematic illustrates the potential mechanism of DSPG@Pep regulating the BMSCs differentiation. Created in BioRender. Dong, H. (https://BioRender.com/4i1zh2t). **i, j** RT-qPCR validation for *IBSP* and *COL4A2*. Error bars represent standard deviation, $n = 3$ independent replicates. ($^{***}p = 3.32 \times 10^{-4}$, $^{***}p = 1.61 \times 10^{-11}$, $^{***}p = 3.17 \times 10^{-10}$; $^{ns}p = 0.444$, $^{**}p = 0.0022$, $^{***}p = 7.91 \times 10^{-4}$). **k** IF staining of integrin β1 and N-cadherin. Scale bar, 20 μm. Statistical analyses were performed with one-way ANOVA, followed by Tukey's multiple comparison post hoc test, $^{*}p < 0.05$, $^{**}p < 0.01$ and $^{***}p < 0.001$. Source data are provided as a Source Data file.

https://doi.org/10.1038/s41467-025-67035-6

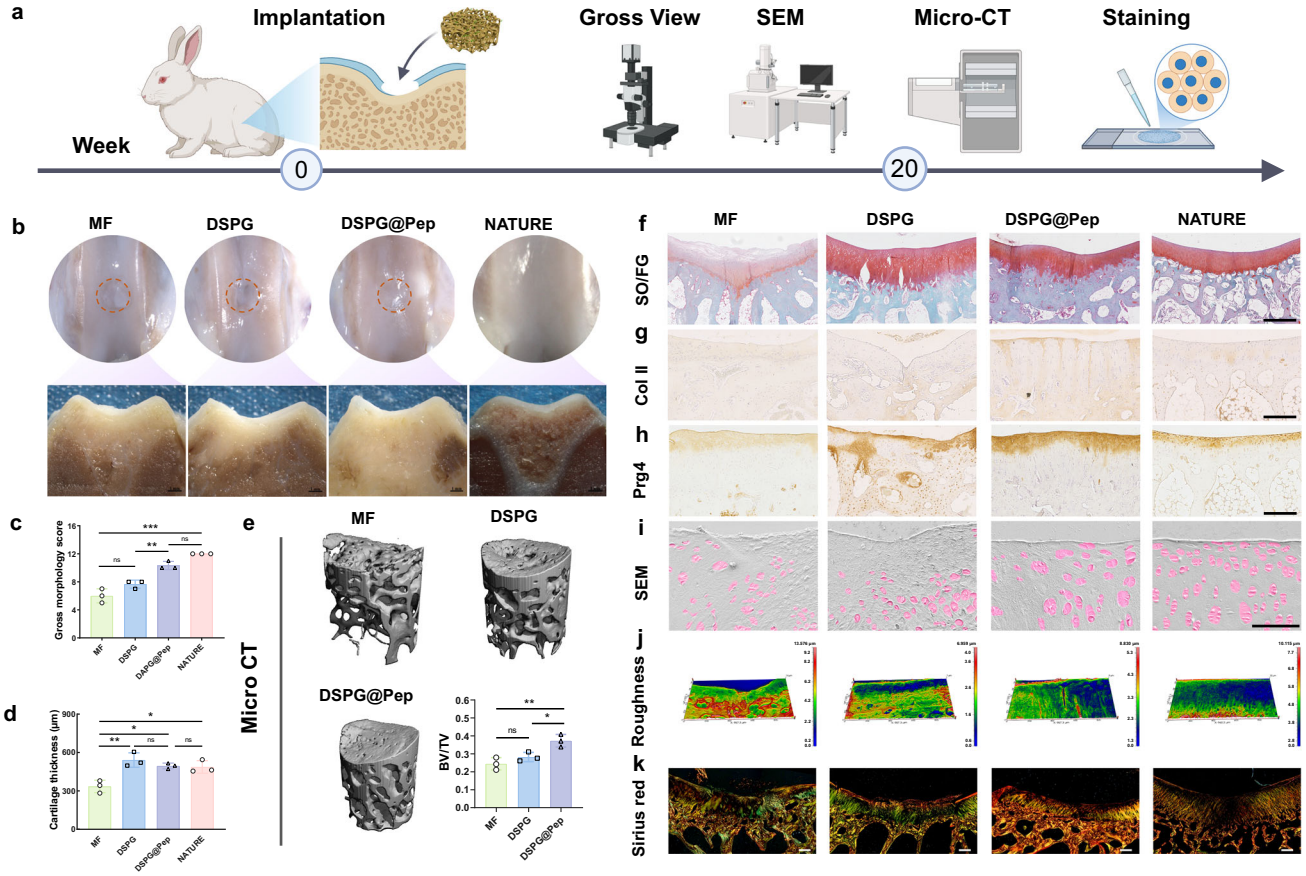

Fig. 5 | DSPG@Pep promotes rabbit endogenous cartilage regeneration. **a** Schematic of rabbit cartilage defect model, material implantation, and post-operative evaluation methods. Created in BioRender. Dong, H. (https://BioRender.com/2pcot5o). **b** Gross view and cross-sectional morphology of rabbit joints at 20 weeks post-surgery. **c** Gross morphology scores. Error bars represent standard deviation, $n = 3$ independent replicates. ($^{ns}p = 0.053$, $^{ns}p = 0.053$, $^{**}p = 4.30 \times 10^{-3}$, $^{***}p = 1.50 \times 10^{-5}$). **d** Statistical analysis of neocartilage thickness. Error bars represent standard deviation, $n = 3$ independent replicates. ($^{*}p = 0.0116$, $^{*}p = 0.0153$, $^{**}p = 0.0025$). **e** Micro-CT evaluation of subchondral bone and BV/TV semi-quantitative analysis at 20 weeks post-surgery. Error bars represent standard deviation, n = 3 independent replicates. ($^{*}p = 0.0314$, $^{**}p = 0.0065$). **f** SO/FG staining results of samples at 20 weeks post-surgery. Scale bar, 500 μm. $n = 3$ independent experiments. **g** Col II IHC staining results. Scale bar, 200 μm. $n = 3$ independent experiments. **h** Prg4 IHC staining results. Scale bar, 200 μm. $n = 3$ independent experiments. **i** SEM images showing morphology and distribution of chondrocytes in cross-sections of regenerated cartilage at 20 weeks post-surgery. Scale bar, 100 μm. $n = 3$ independent experiments. **j** Contour profiles and surface roughness quantification of regenerated cartilage cross-sections. $n = 3$ independent experiments. **k** Sirius Red staining demonstrating collagen fiber type and arrangement in regenerated cartilage. Scale bar, 250 μm. $n = 3$ independent experiments. Statistical analyses were performed with one-way ANOVA, followed by Tukey's multiple comparison post hoc test, $^{*}p < 0.05$, $^{**}p < 0.01$ and $^{***}p < 0.001$. Source data are provided as a Source Data file.

ossification, but DSPG@Pep effectively reduced the integrin-mediated scaffold-cell interactions sites to reverse ossification risk.

DSPG@Pep promotes rabbit endogenous cartilage regeneration

In order to evaluate the ability of promoting endogenous cartilage regeneration, a rabbit knee full-thickness cartilage defect model combined with MF was established (Fig. 5a). Samples were collected after 6 and 20 weeks. At 20 weeks after surgery, the defects in DSPG@Pep group were completely covered by the neocartilage, with the intact integration between regenerated and native cartilage (Fig. 5b). The macroscopic evaluation scores (Fig. 5c) in DSPG@Pep group surpassed those of the microfracture (MF) and DSPG groups. Meanwhile, the cartilage thickness was also greater than that of MF group, and had no significant difference from that of natural group (Fig. 5d). Micro-CT (Fig. 5e) analysis showed some collapse of the subchondral bone in the MF group, whereas the DSPG and DSPG@Pep groups maintain the structural integrity. Notably, DSPG@Pep demonstrated the highest bone volume/total volume (BV/TV) ratio, indicating enhanced osteochondral protection.

Histological assessments via safranin O-fast green (SO/FG) staining (Fig. 5f) and immunohistochemical (IHC) staining of Col II (Fig. 5g) confirmed hyaline-like cartilage regeneration in the DSPG@Pep group. Further Prg4 IHC (Fig. 5h) suggested that the neocartilage of the DSPG@Pep group had the potential to lubricate the reconstructed joint. As we all known, the morphology of chondrocytes in native cartilage tissue presents gradient changes. Therefore, SEM (Fig. 5i) was used to observe the distribution and morphology of chondrocytes in regenerated cartilage. The morphology and arrangement of chondrocytes in DSPG@Pep group were the closest to those of native cartilage. Surface profilometry (Fig. 5j) further revealed a comparable low roughness of neocartilage in DSPG@Pep. However, the roughness of MF group was the highest, which might be attributed to the fibrocartilage formation after MF. Sirius red staining (Fig. 5k) further manifested that the collagen fibers are arranged approximately perpendicular to the surface of the cartilage in DSPG@Pep group, in contrast with the random orientation observed in the MF group. In addition, the results of SO/FG, Col II staining and the mechanical test (Supplementary Fig. 10a-c) at 6 and 20 weeks illustrated that the DSPG and DSPG@Pep had more complete structure and mechanical

properties in comparison with the MF group. Notably, the morphology and mechanical properties of the regenerated cartilage tissue both in DSPG and DSPG@Pep group gradually improved from 6 to 20 weeks, especially DSPG@Pep group. These multimodal evaluations collectively demonstrated that DSPG@Pep displayed good potential for promoting articular cartilage regeneration.

DSPG@Pep improves endogenous cartilage regeneration of pigs

The full-thickness cartilage defect model in conjunction with MF in Bama pig was utilized to evaluate the property of DSPG@Pep to promote endogenous cartilage regeneration in large animals (Fig. 6a and Supplementary Fig. 11a). After the material was implanted, the patella was repositioned and the joint movement was simulated. It was found that the material could be fixed at the defect site (Supplementary Movie. 1). At 5 months after surgery, the cartilage defects of DSPG@Pep group were covered by the neocartilage, whereas only partial filling was observed in the MF group (Fig. 6b and Supplementary Fig. 11b). The CT results (Fig. 6c and Supplementary Fig. 11c) revealed that the damage of subchondral bone was more serious in MF group, whereas DSPG@Pep to some extent rescued the persistent damage of subchondral bone. MRI images (Fig. 6c and Supplementary Fig. 11d) indicated stronger signals from the neocartilage in the DSPG@Pep group, with a smooth and continuous surface, while swelling might be present in both the neocartilage and subchondral bone in the MF group. Furthermore, histological staining was employed to assess the matrix secretion and fiber arrangement of the neocartilage. Hematoxylin and eosin (H&E) (Supplementary Fig. 11e), SO/FG (Fig. 6d), Col II IF (Fig. 6e), and Sirius red (Fig. 6f) staining demonstrated the formation of a hyaline-like cartilage matrix in the DSPG@Pep group, with the fiber arrangements approaching those of native cartilage. These findings confirmed the ability of DSPG@Pep to promote the cartilage regeneration in large animals.

Discussion

Herein, we developed artificial proteoglycan assemblies with anti-swelling property and self-activating biofunctions through simulating the structural and functional regulation mechanism of the natural cartilage matrix (Fig. 1). By emulating the core protein-HA-collagen fiber interactions to constrain and stabilize natural proteoglycan aggregates, DSPG@Pep overcomes the limitations of conventional biomimetic materials in terms of structural stability and self-activating biofunctions. Furthermore, the introduction of bioactive peptides achieves endogenous stem cell recruitment, directed chondrogenic differentiation, and ossification downregulation. This strategy offers a promising solution for endogenous cartilage regeneration after MF (Fig. 6g).

Conventional biomimetic materials for cartilage regeneration focus primarily on mimicking matrix components (e.g., collagen and HA) and gradient architectures, but fail to restore the mechanical stability and biofunctions of native cartilage[33–35]. In our previous research, the co-assembled hydrogel prepared by the "molecular Velcro"-inspired peptide and gelatin co-assembly strategy was suitable for loading and protecting exogenous BMSCs to promote cartilage regeneration due to the high β-sheet content and compressive strength[36]. This confirmed that simulating the advanced structure of natural proteins to reproduce the biofunctions is a feasible strategy. While, the DSPG@Pep in this study is a cell-free scaffold developed for Microfracture (MF), which can resist swelling and degradation after bone marrow blood infiltration, as well as promote endogenous BMSCs recruitment and cartilage regeneration. In addition, this research conducted a more in-depth exploration on the regulation of differentiation behavior by scaffolds, and verified the feasibility of this strategy in large animal models. Specifically, inspired by the restriction of collagen fibers on PGs and biofunctions of natural cartilage, DSPG@Pep was fabricated by physical and chemical driven co-assembly of peptide, SFD and HASH (Fig. 2a). It demonstrated obvious advantages in the early postoperative period: relieving the physiological compressive stress to provide stable mechanical support for regeneration microenvironment, preventing structural instability after bone marrow blood infiltration, which achieved stably immobilization in the defects (Supplementary Movie. 1). Fluorescence staining of calcium ion and transcriptomic analysis further revealed that the DSPG@Pep not only enhanced cell recruitment but also suppressed the genes expression associated with calcium signaling pathway and ossification (Fig. 3a-g and Fig. 4a-h). Compared with other traditional biomimetic materials, this design concept is more refined. It not only meets the biomimetic requirements of components but also mimics the restrictive effect of collagen fibers on proteoglycans at the molecular assembly level to endows it with structural stability. It also mimics ECM-mediated cell behavior, which realize the endogenous activation and regulation. Such multi-dimensional biomimetic integration and regulation are of great importance for inducing cartilage regeneration after MF.

Notably, many studies have confirmed that ossification could be promoted by facilitating calcium influx, upregulating the calcium signaling pathway, and activating voltage-gated calcium ion channels[37,38]. In our study, we found that the introduction of this peptide simultaneously down-regulated the DSPG-induced ossification trend by decreasing the cytosolic calcium concentration, while enhanced stem cells recruitment. These findings align closely with the biological mechanisms of endochondral ossification and cartilage calcification in osteoarthritis: ion imbalance can induce crystal nucleation and growth, especially elevated intracellular concentrations of calcium ion, resulting in pathological calcification and ossification[39,40]. Therefore, we speculated that DSPG@Pep might regulate calcium signaling pathway through functional peptides to reduce cytosolic calcium concentration, thereby inhibiting ossification to assist chondrogenic differentiation (Fig. 4h). This "pro-recruitment and anti-ossification" dual-regulatory function provides a critical safeguard for maintaining the hyaline cartilage phenotype.

Rabbit and pig articular cartilage defects models confirmed the significant regenerative ability of DSPG@Pep. Both the early recruitment of stem cells after surgery and the later cartilage regeneration were superior to those of MF group (Fig. 3f-g and Fig. 5). Studies have shown that the interface between cartilage and subchondral bone plays important roles in transferring load and maintaining articular cartilage and subchondral bone as independent physiological environments[41]. Here, we found the interfacial structure between the neocartilage and subchondral bone was more intact in the pig model (Fig. 6c, d). In addition, the fiber alignment of regenerative collagen closely resembled with native cartilage (Fig. 6e, f). These satisfactory phenomena might be attributed to the early structural stability, stem cell recruitment and ossification inhibition. This dependency solely on inducible biomaterials to trigger cartilage regeneration resolved the challenges of limited cell sources, avoided the complexities and clinical risks associated with exogenous transplantation of cell, factors and drugs. Despite significant progress made in this study, further evaluation through long-term animal experiments is necessary to assess long-term stability of regenerated cartilage and the matching relation between degradation and regeneration. Additionally, the specific target points within the calcium signaling pathway and their interactions with chondrogenic differentiation-related signals require deeper analysis.

Overall, this study developed artificial proteoglycan assemblies with structural stability and self-activation by combining biomimetic design with self-activating biofunctions. DSPG@Pep efficiently induced endogenous cartilage regeneration and hyaline cartilage phenotype maintenance via stabilizing the mechanical microenvironment, recruiting endogenous stem cells, and downregulating ossification. Pig model confirmed its notable advantages in restoring

https://doi.org/10.1038/s41467-025-67035-6

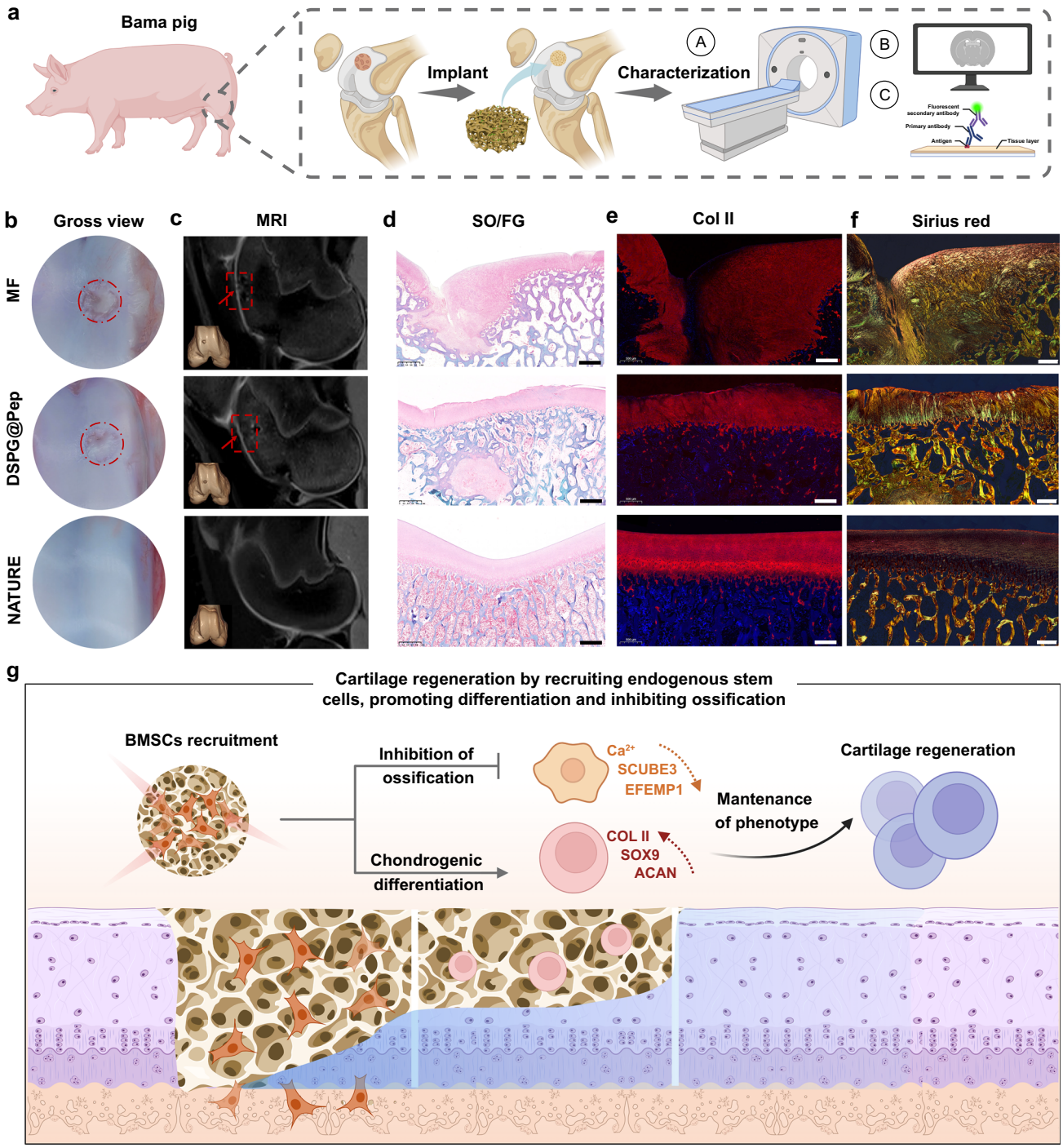

Fig. 6 | DSPG@Pep promotes endogenous cartilage regeneration of pigs. **a** Schematic of the implantation and subsequent characterization methods. Created in BioRender. Dong, H. (https://BioRender.com/9g4uaoc). **b** Gross view at 5 months post-surgery. **c** Micro-CT and MRI images evaluate the regeneration of subchondral bone and cartilage. Red dashed boxes represent defects; red arrows represent the repaired cartilage. **d** SO/FG staining assessing GAG secretion in neocartilage. Scale bar, 1 mm. $n = 3$ independent experiments. **e** Col II IF staining of neocartilage. Scale bar, 500 μm. $n = 3$ independent experiments. **f** Sirius Red staining demonstrating collagen fiber type and arrangement. Scale bar, 500 μm. $n = 3$ independent experiments. **g** Summary: DSPG@Pep promotes articular cartilage regeneration by recruiting endogenous stem cells, promoting chondrogenic differentiation, and downregulating calcium signaling pathway and ossification. Created in BioRender. Dong, H. (https://BioRender.com/7j56yos).

cartilage structure and biofunction, providing a promising design strategy of endogenous cartilage regenerative biomaterials.

Methods

Animals

6 Sprague-Dawley rats (SD rats, 250-300 g) were bred in one cage (30 cm x 50 cm x 25 cm) under standard conditions with ad libitum access to food and water under a 12/12 h light/dark cycle. The laboratory room was quiet and well-ventilated, avoiding direct strong light and noise interference. Iodophor was used to disinfect the wound continuously for 3 days after the experiment. In case of any abnormal phenomenon in animals, the veterinarian would immediately provide diagnosis and nursing treatment. For experimental rats that cannot be cured, euthanasia was performed

by injecting lidocaine and pentobarbital sodium into the enterocoelia.

24 male Oryctolagus cuniculus (New Zealand white rabbits, 2.5-3 kg, 2.5–3 months old) were obtained from Chengdu Dossy Experimental Animals Co., Ltd. (Chengdu, China) and fed with standard laboratory chow (GB14924.3-2010, Chengdu Dossy Experimental Animals Co., Ltd., China) under constant conditions (25 ± 2 °C, 55 ± 2% relative humidity, 12/12 h light/dark cycle). Each rabbit was kept alone in a separate cage (42 cm x 50 cm x 35 cm). Three days after the surgery, iodophor was used to disinfect the wound every day, and gentamicin was injected once a day to prevent infection of the wound. In case of any abnormal phenomenon in animals, the veterinarian would immediately provide diagnosis and nursing treatment. For experimental rabbits that cannot be cured, euthanasia was performed by injecting pentobarbital sodium into the vein.

3 male bama pigs were bought from Pizhou Dongfang Breeding Co., Ltd. (Pizhou, China) and fed with formulated feed for miniature pigs (24022211, Beijing Keao Xieli Feed Co.,Ltd.). Feed the pigs once in the morning and afternoon every day, and check the remaining food. Automatic water supply system was provided. Each pig was kept alone in a separate cage (150 cm x 150 cm x 150 cm) under constant conditions (18-22 °C, 40-70% relative humidity, 12/12 h light/dark cycle). During the surgery, the patient monitor was used to continuously monitor the oxygen saturation, heart rate and blood pressure, with proper airway alignment maintained throughout the procedure. Three days after the surgery, iodophor was used to disinfect the wound every day, and give cefixime and etoricoxib tablets twice a day to relieve pain. All the pigs were monitored daily for mental state, appetite, wound healing and activity. In case of any abnormal phenomenon in animals, the veterinarian would immediately provide diagnosis and nursing treatment. At the end of study, euthanasia was carried out by injecting pentobarbital sodium into the vein.

Synthesis and characterization of HASH and SFD

The synthesis of HASH was as follows. Initially, sodium hyaluronate (HA, 340 kDa, 400 mg, Shandong Huaxi Biotech Co., Ltd.) was dissolved in ultrapure water, the N-hydroxysuccinimide (NHS, 230 mg, Best-reagent Corporation, Chengdu, China) and 1-Ethyl-3-(3-dimethyllaminopropyl) carbodiimide hydrochloride (EDCI, 959 mg, Best-reagent Corporation, Chengdu, China) were added, with controlling pH at 4.75–5.00 to activate the carboxyl groups. Then, cysteamine hydrochloride (CSA·HCl, 570 mg, Best-reagent Corporation, Chengdu, China) was added to react for 10–12 h under the same pH conditions. Afterwards, the mixed solution was dialyzed and lyophilized. Similarly, SFD was synthesized as follows. The SF solution was extracted from Bombyx mori L. cocoons by degumming and dissolving in 9.3 M lithium bromide (LiBr) solution at 60 °C for 4 h. After dialyzing, the SF solution (1 g, 150 mL), NHS (230 mg), EDCI (959 mg), and dopamine hydrochloride (Sigma-Aldrich, 190 mg) were mixed to react for 24 h under pH 4.75 ~ 5.00 and N_2 atmosphere protection. Subsequently, the solution was dialyzed and stored at 4 °C. The ^{1}H NMR spectrum (400 Hz, Bruker AMX-400, USA) was used to determine the grafting efficiency of thiols. Fourier transform infrared (FT-IR) spectroscopy was conducted on a Nexus 670 spectrometer with a 2 cm^{-1} resolution in the wavenumber range of 400–4000 cm^{-1} for SFD analysis.

Preparation and characterization of DSPG

Firstly, solutions of SF, SFD, SFHS, SFDHS, SPG and DSPG at a concentration of 1 mg/mL were prepared and observed under TEM (TECNAIG2 F20 S-TWIN at 200 kV). Similarly, solutions at a concentration of 0.75 mg/mL were prepared for AFM imaging. ζ-Potential of SF, SFD and HASH (1 mg/mL) was measured by Malvern Zetasizer Nano ZS instrument (Malvern Instrument, Worcestershire, UK). Thioflavin T fluorescent probe was used to stain β-sheet conformations in SF, SFD, SFHS, SFDHS, SPG, DSPG by measuring the fluorescence intensity with excitation wavelength at 420 nm and emission wavelength at 528 nm. ITC was used to evaluate the intermolecular interactions. Meanwhile, hydrogels (SPG or DSPG) were prepared by adjusting solution (30 mg/mL) pH to 7, and observed under confocal lasers canning microscopy (CLSM) by rhodamine-phalloidin staining. At the same time, circular dichroism (CD) spectroscopy and analysis was used to examine the secondary structure of SPG and DSPG with sample concentration at 0.1 mg/mL, wavelength range from 180–260 nm and a 2 cm^{-1} resolution.

The hydrogels were lyophilized to obtain sponge-like SPG and DSPG. Initially, the Effective Young's Modulus was measured using a nanoindentation instrument (Piuma, Xuan Yuan Technology Co., Ltd.). Subsequently, the swelling ratio (M1:M0, periodic weight measurements, initial weight) was calculated by immersing the sponge-like SPG and DSPG in PBS solution, with photographic documentation tracking dimensional changes. Dynamic mechanical analyzer (DMA, TA-Q800, USA) was used to test compression stress-strain characteristics. FT-IR spectroscopy with deconvolution analysis was employed to assess secondary structure alterations. Concurrently, β-sheet distribution was observed by CLSM after Thioflavin T fluorescence staining. Five sponge-like DSPG groups with different volume ratios including DSPG (1: 4), DSPG (1: 2), DSPG (1: 1), DSPG (2: 1), DSPG (4: 1) were fabricated for performance optimization. SEM characterized internal pore architecture and porosity. Key parameters including dimensional expansion rate, swelling rate, and degradation rate in PBS solution of hyaluronidase (100 U/mL) were systematically evaluated. Storage modulus and loss modulus were quantified by DMA. The in vivo swelling and degradation properties were evaluated using a subcutaneous implant model in Sprague-Dawley rats (SD rats).

Preparation and characterization of DSPG@Pep

Mal-PEG-NHS (Ponsure Biological) was employed as the intermediate active macromolecule for conjugating DSPG with a bioactive peptide (EPLQLKMC, Scilight-Peptide Beijing). The sponge-like DSPG was immersed in a 2 mg/mL Mal-PEG-NHS solution and incubated under shaking conditions at 37 °C for 1 h at pH 7-8.5. Subsequently, the sponge was transferred into a 0.1 mg/mL solution of the peptide, reacted for 24 h at 4 °C under pH 6.5-7.5, washed with PBS and lyophilized for further use. FT-IR and XPS evaluated the grafting efficiency of peptide. The effects of peptide grafting on pore structure and porosity were investigated by SEM. A PBS solution of FITC-BSA was dropped onto the material surface, and the penetration depth of FITC-BSA was observed using CLSM after 1 min to assess the impact on mass transfer. Additionally, DMA was utilized to test changes in storage modulus, loss modulus, and compressive stress-strain behaviors.

Evaluation of biocompatibility and cell recruitment performance

BMSC was extracted from the newborn New Zealand rabbit as our previous study[42]. Rabbit BMSC was maintained in complete αMEM media containing 10% fetal bovine serum (FBS) and 1% penicillin/streptomycin (PS) and cultured at 37 °C in a cell culture incubator with 5% CO_2. The second passage (P_2) BMSCs were trypsinized using 0.05% trypsin (Gibco) and resuspended to a specific concentration, then added dropwise onto the surfaces of SPG, DSPG and DSPG@Pep. After incubation, chondrogenic differentiation medium was added to each well of the 24-well plate, with changing every two days. On the third day, cell viability was assessed using FDA/PI staining and observed by CLSM. Cell spreading was evaluated using Rhodamine-phalloidin/DAPI staining and also visualized under CLSM. The proliferation of cells on the materials was measured using a CCK-8 assay kit.

The BMSC recruitment capability was evaluated using Transwell model (pore size: 8 μm) and scratch assay. In the Transwell model, cells were cultured in the upper chamber for 24 h. Subsequently, they were fixed and stained with crystal violet followed by semi-quantitative

analysis to assess the vertical migration quantity of cells. For the scratch assay, the horizontal migration ability was examined by calculating the healing rate after 10 h.

Moreover, cartilage defects were created in adult New Zealand white rabbits, followed by MF. Then, DSPG and DSPG@Pep were implanted into the defect sites. At seven days post-operation, the samples were retrieved. Immunofluorescence (IF) staining was employed to evaluate the endogenous stem cell recruitment capacity in vivo.

Influence of SPG/DSPG/DSPG@Pep on chondrogenic differentiation of BMSCs in vitro

BMSCs were seeded onto the surfaces of materials and then cultured in chondrogenic induction medium with changing every two days. After 21 days, the cultured samples were collected and analyzed for their effects on the chondrogenic differentiation of BMSCs in vitro by employing safranin o staining, Col II and Col II IF staining, glycosaminoglycan (GAG)/DNA quantitative detection kit, and Quantitative Real-time PCR (RT-qPCR) analysis. The specific procedures were as follows.

The samples were fixed with 4% paraformaldehyde, embedded in paraffin and sliced for later use. After the dewaxing and rehydration step, SO-FG (G1371, Solarbio) was used for staining. For the IF staining, after being treated with 0.2% Triton X-100 and blocked with goat serum, samples were incubated with primary antibodies Col II (BA0533, Boster) and Col X (BA2023, Boster), followed by secondary antibody Goat Anti-Rabbit IgG H&L (ab150080, Abcom) staining, and finally with DAPI for nuclei staining. Finally, A slide scanner (Evident VS200, Olympus) was applied to view the images.

The quantitative detection of GAG/DNA was performed as follows. First, the samples were digested in a papain solution prepared in phosphate buffer at 65 °C overnight. After centrifugation at 13523 xg for 10 min at 4 °C, the supernatant was collected. The GAG content was determined using the Blyscan GAG assay kit (B100, Biocolor, U.K.), while DNA quantification was conducted with Hoechst 33258 fluorescent dye (B1302, Sigma-Aldrich, China). Data were calculated using standard calibration curve equations and presented as the ratio of GAG to DNA.

The RT-qPCR procedure was as follows. Before RNA extraction, the samples were washed twice with PBS solution, transferred to a tissue crushing tube, and Buffer RLT was added, which was broken by a tissue homogenizer. The RNeasy Mini Kit (74104, Qiagen) was used to extract the RNA and concentration was determined (Nano Drop 2000). Then the RNA was reverse transcribed into cDNA using the iScript™ cDNA Synthesis Kit (Bio-Rad). SsoFastTM EvaGreen Supermix (BIO-RAD) was used to conduct RT-qPCR that performed on a CFX96 Touch™ Real-Time PCR Detection System (BIO-RAD). The expression levels of *Sox9, Acan, Col II, Col X* and *Col I* were evaluated, and the primers (Tsingke Biotechnology Co., Ltd.) were listed in Table S1. All the expressions of other genes were calculated on the basis of the expression level of *GAPDH*.

RNA sequencing and validation

Using the same method described above, BMSCs were seeded on the surface of the materials and then cultured in chondrogenic induction medium with fluid change every two days. After 14 days, samples were collected and stored in liquid nitrogen. Transcriptome analysis was performed by Novogene, Inc. Firstly, RNA was extracted, and RNA degradation and contamination were monitored on 1% agarose gels. Total RNA was used as input material for the RNA sample preparations. The clustering of the index-coded samples was performed on a cBot Cluster Generation System using TruSeq PE Cluster Kit v3-cBot-HS (Illumia) according to the manufacturer's instructions. After cluster generation, the library preparations were sequenced on an Illumina Novaseq platform and 150 bp paired-end reads were generated. Raw data (raw reads) of fastq format was processed through in-house Perl scripts. Differential expression analysis of two conditions/groups (3 biological replicates per condition) was performed using the DESeq2 R package (1.20.0). FPKM method was adopted to determine gene expression. Significant analysis was performed using the p-value and false discovery rate (FDR) analysis. Meanwhile, differentially expressed genes were determined as fold change > 2 or fold change <0.5, FDR < 0.05. Finally, representative gene expression of *CACNA1G*, *AVPRV1A*, *PLCB1*, *RET*, *MST1R*, *RYR3*, *EFEMP1*, *SCUBE3*, *SPARCL1*, *COL4A2, IBSP and TNC* was evaluated via RT-qPCR as mentioned above, and the primers (Tsingke Biotechnology Co., Ltd.) were listed in Table S1. At the same time, calcium ions in the cytoplasm were labeled with a calcium ion fluorescence probe (S1060, Beyotime), and observed under CLSM. Immunofluorescent staining (IF) was used to assess the clustering of integrin β1 and N-cadherin.

The evaluation of rabbit cartilage regeneration

The rabbits were anesthetized with 3% sodium pentobarbital solution. A critical-sized full-thickness cartilage defect (4 mm in diameter) was created using a trephine, followed by MF. The implant material was then inserted into the defect site, and the incision was sutured. Gentamicin sulfate (2 mL) was administered daily for three consecutive days post-surgery. Euthanasia was performed at 6 and 20 weeks post-operation. The surface and cross section of the defects were photographed and recorded with an asthenic microscope (SZx7, Olympus, Japan), and the average thickness of the neocartilage was measured. According to the International Cartilage Repair Society (ICRS) histological scoring system (Table S2), the gross view of neocartilage was scored. Micro-CT was used to with a resolution of 15 μm. After 3D reconstruction, BV/TV values were calculated to compare subchondral bone regeneration in each group. Subsequently, the samples were fixed in 4% paraformaldehyde and decalcified with EDTA decalcified solution. After complete decalcification, Safranin O-Fast Green (SO/FG) (G1371, Solarbio) and Sirius red (PH1098, Scientific PHYGENE) staining was applied. IHC staining of Col II (1: 500, NB600-844, NOVUS) and Prg4 (1: 500, MABT401, Sigma-Aldrich) was performed to evaluate the structure of regenerated cartilage and secretion of specific matrix. Subsequently, optical profilometer (Contour4GT-K, Bruker Germany) and SEM were used to observe the microscopic morphology and cell arrangement of the regenerated cartilage. Biological nanoindenter (Optics11, Netherlands) was utilized to measure the Effective Young's modulus of regenerated cartilage.

The evaluation of cartilage regeneration in pigs

Three Bama pigs (male, 35–40 kg, 9 months old, with 3 parallel samples in each group) were anesthetized and underwent knee arthrotomy through anteromedia parapatellar incision and patella eversion. A full-layer cartilage defect with a diameter of 8 mm was created on the lateral trochlear groove of distal femur of knee joint, and MF was performed. After the material was implanted, the patella was reset, the joint was moved to check whether the material had fallen off, and the flesh was sutured to ensure that it had not fallen off. Antibiotics were given for three consecutive days after surgery. Five months later, Bama pigs were euthanized. CT (uCT760, UNITED IMAGING, China) was used to observe the subchondral bone, and MRI scanner (uMR780, UNITED IMAGING, China) was used to observe the cartilage repair. The samples were further fixed with 4% paraformaldehyde, decalcified with 10% EDTA decalcified solution, embedded in paraffin and sliced for later use. Hematoxylin and eosin (H&E) staining was used to evaluate the morphological attributes of the tissue. GAG deposition was analyzed using SO/FG staining. IF staining of Col II was used to evaluate the type of neocartilage. The type and arrangement of collagen fibers were analyzed by Sirius red staining (PH1098, Scientific PHYGENE).

Statistical analysis

All data were expressed as means ± standard deviation of three representative experiments. Parametric statistics were conducted

using GraphPad Prism software (GraphPad Software Inc.) by Student's t-test (unpaired and two-tailed) and one way analysis of variance (ANOVA), followed by Tukey's multiple comparison post hoc test. The values were considered significantly different when $p < 0.05$.

Ethical statement

This study complies with all applicable ethical regulations. All animal studies in this research were approved by the Sichuan University Medical Ethics Committee (approval number: KS20240262). All animal procedures were performed in accordance with the guidelines for care and use of Laboratory Animals of Sichuan University (approval number: KS20240262).

Reporting summary

Further information on research design is available in the Nature Portfolio Reporting Summary linked to this article.

Data availability

Source data are provided with this paper. The source data of figures generated in this study are provided in the Source Data file. The Supplementary data generated in this study are provided in the Supplementary Information. The transcriptome sequencing data generated in this study have been deposited in the National Center for Biotechnology Information Sequence Read Archive under accession code PRJNA1322321. Source data are provided with this paper.

References

1. Murphy, M. P. et al. Articular cartilage regeneration by activated skeletal stem cells. *Nat. Med.* **26**, 1583–1592 (2020).
2. Li, J. et al. Articular fibrocartilage-targeted therapy by microtubule stabilization. *Sci. Adv.* **8**, eabn8420 (2022).
3. Kwon, H. et al. Surgical and tissue engineering strategies for articular cartilage and meniscus repair. *Nat. Rev. Rheumatol.* **15**, 550–570 (2019).
4. DeMoya, C. D. et al. Advances in viscosupplementation and tribosupplementation for early-stage osteoarthritis therapy. *Nat. Rev. Rheumatol.* **20**, 432–451 (2024).
5. Maroudas, A. & Venn, M. Chemical composition and swelling of normal and osteoarthritic femoral head cartilage. II. swelling. *Ann. Rheum. Dis.* **36**, 399–406 (1977).
6. Kiani, C., Chen, L., Wu, Y. J., Yee, A. J. & Yang, B. B. Structure and function of aggrecan. *Cell Res.* **12**, 19–32 (2002).
7. Wang, W. et al. Assembling custom side chains on proteoglycans to interrogate their function in living cells. *Nat. Commun.* **11**, 5915 (2020).
8. Jin, H.-J. & Kaplan, D. L. Mechanism of silk processing in insects and spiders. *Nature* **424**, 1057–1061 (2003).
9. Kim, T., Kim, B. J., Bonacchini, G. E., Ostrovsky-Snider, N. A. & Omenetto, F. G. Silk fibroin as a surfactant for water-based nanofabrication. *Nat. Nanotechnol.* **19**, 1514–1520 (2024).
10. Reizabal, A., Costa, C. M., Pérez-Álvarez, L., Vilas-Vilela, J. L. & Lanceros-Méndez, S. Silk fibroin as sustainable advanced material: material properties and characteristics, processing, and applications. *Adv. Funct. Mater.* **33**, 2210764 (2023).
11. Zhang, X., Xiao, L., Ding, Z., Lu, Q. & Kaplan, D. L. Engineered tough silk hydrogels through assembling β-sheet rich nanofibers based on a solvent replacement strategy. *ACS Nano* **16**, 10209–10218 (2022).
12. Choi, W. et al. Templated assembly of silk fibroin for a biofeedstock-derived heart valve leaflet. *Adv. Funct. Mater.* **34**, 2307106 (2024).
13. Zhang, Y. et al. Natural silk spinning-inspired meso-assembly-processing engineering strategy for fabricating soft tissue-mimicking biomaterials. *Adv. Funct. Mater.* **32**, 2200267 (2022).
14. Kahle, E. R. et al. Molecular engineering of pericellular microniche via biomimetic proteoglycans modulates cell mechanobiology. *ACS Nano* **16**, 1220–1230 (2022).
15. Lee, J. et al. Micromechanical property mismatch between pericellular and extracellular matrices regulates stem cell articular and hypertrophic chondrogenesis. *Matter* **6**, 475–492 (2023).
16. Ma, Z. et al. Smart μ-fiber hydrogels with macro-porous structure for sequentially promoting multiple phases of articular cartilage regeneration. *Adv. Funct. Mater.* **32**, 2113380 (2022).
17. Miao, Y. et al. Double-network DNA macroporous hydrogel enables aptamer-directed cell recruitment to accelerate bone healing. *Adv. Sci.* **11**, 2303637 (2024).
18. Zhou, D., Yan, X., Xiao, L., Wang, J. & Wei, J. Gold capped mesoporous bioactive glass guides bone regeneration via BMSCs recruitment and drug adaptive release. *Chem. Eng. J.* **487**, 150546 (2024).
19. Zhang, W. et al. Tannic acid-mediated dual peptide-functionalized scaffolds to direct stem cell behavior and osteochondral regeneration. *Chem. Eng. J.* **396**, 125232 (2020).
20. Zhang, W. et al. An all-silk-derived functional nanosphere matrix for sequential biomolecule delivery and in situ osteochondral regeneration. *Bioact. Mater.* **5**, 832–843 (2020).
21. Zhu, M., Zhong, W., Cao, W., Zhang, Q. & Wu, G. Chondroinductive/chondroconductive peptides and their-functionalized biomaterials for cartilage tissue engineering. *Bioact. Mater.* **9**, 221–238 (2022).
22. Sato, K., Hendricks, M. P., Palmer, L. C. & Stupp, S. I. Peptide supramolecular materials for therapeutics. *Chem. Soc. Rev.* **47**, 7539–7551 (2018).
23. Kumar, V. A. et al. Treatment of hind limb ischemia using angiogenic peptide nanofibers. *Biomaterials* **98**, 113–119 (2016).
24. Zhang, C. et al. Supramolecular nanofibers containing arginine-glycine-aspartate (RGD) peptides boost therapeutic efficacy of extracellular vesicles in kidney repair. *ACS Nano* **14**, 12133–12147 (2020).
25. Guo, Q. et al. Dynamic proteinaceous hydrogel enables in-situ recruitment of endogenous TGF-β1 and stem cells for cartilage regeneration. *Adv. Funct. Mater.* **34**, 2403055 (2024).
26. Bian, X. et al. Amino acid surfactant-induced superfast gelation of silk fibroin for treating noncompressible hemorrhage. *Adv. Funct. Mater.* **32**, 2207349 (2022).
27. Qin, X. et al. Cell-matrix adhesion and cell-cell adhesion differentially control basal myosin oscillation and Drosophila egg chamber elongation. *Nat. Commun.* **8**, 14708 (2017).
28. Zhang, Z. et al. Programmable integrin and N-cadherin adhesive interactions modulate mechanosensing of mesenchymal stem cells by cofilin phosphorylation. *Nat. Commun.* **13**, 6854 (2022).
29. Wu, K. et al. Exosomal miR-19a and IBSP cooperate to induce osteolytic bone metastasis of estrogen receptor-positive breast cancer. *Nat. Commun.* **12**, 5196 (2021).
30. Reagan, M. R. et al. Microrna-dependent modulation of osteogenesis in a 3D in vitro bone marrow model system of multiple myeloma. *Blood* **122**, 3093–3093 (2013).
31. Jeanne, M., Jorgensen, J. & Gould, D. B. Molecular and genetic analyses of collagen type IV mutant mouse models of spontaneous intracerebral hemorrhage identify mechanisms for stroke prevention. *Circulation* **131**, 1555–1565 (2015).
32. Song, L. et al. Bone marrow-derived tenascin-c attenuates cardiac hypertrophy by controlling inflammation. *J. Am. Coll. Cardiol.* **70**, 1601–1615 (2017).
33. Zhao, Z. et al. Cartilage-inspired self-assembly glycopeptide hydrogels for cartilage regeneration via ROS scavenging. *Bioact. Mater.* **32**, 319–332 (2024).
34. Lee, J., Lee, S., Huh, S. J., Kang, B.-J. & Shin, H. Directed regeneration of osteochondral tissue by hierarchical assembly of spatially organized composite spheroids. *Adv. Sci.* **9**, 2103525 (2022).

35. Feng, Q. et al. Injection and self-assembly of bioinspired stem cell-laden gelatin/hyaluronic acid hybrid microgels promote cartilage repair in vivo. *Adv. Funct. Mater.* **29**, 1906690 (2019).
36. Zhao, C. et al. Molecular co-assembled strategy tuning protein conformation for cartilage regeneration. *Nat. Commun.* **15**, 1488 (2024).
37. Han, Z. et al. Microenvironmentally enhanced supramolecular hydrogels reverse multiple dilemmas in bone infection. *Mater. Today* **82**, 32–48 (2025).
38. Camarero-Espinosa, S. & Moroni, L. Janus 3D printed dynamic scaffolds for nanovibration-driven bone regeneration. *Nat. Commun.* **12**, 1031 (2021).
39. Kronenberg, H. M. Developmental regulation of the growth plate. *Nature* **423**, 332–336 (2003).
40. Bernabei, I., So, A., Busso, N. & Nasi, S. Cartilage calcification in osteoarthritis: mechanisms and clinical relevance. *Nat. Rev. Rheumatol.* **19**, 10–27 (2023).
41. Koh, R. H. et al. Bioceramic-mediated chondrocyte hypertrophy promotes calcified cartilage formation for rabbit osteochondral defect repair. *Bioact. Mater.* **40**, 306–317 (2024).
42. Li, Z. et al. Bioinspired polysaccharide hybrid hydrogel promoted recruitment and chondrogenic differentiation of bone marrow mesenchymal stem cells. *Carbohydr. Polym.* **267**, 118224 (2021).

Acknowledgements

The authors disclose support for the research of this work from Guolong Meng, Lingzhu Yu, and Jiao Lu (National Engineering Research Center for Biomaterials, Sichuan University) for helping in characterizing AFM and CLSM. The authors disclose support for the research of this work from the National Natural Science Foundation of China [Nos. 32422044 and 52473141] (Y.S.) and Sichuan Provincial Natural Science Foundation of China [No. 2025NSFJQ0034] (Y.S.).

Author contributions

Z.L.L., M.D.Z. and J.Y.Z.: Conceptualization, Data curation, Formal analysis, methodology, writing-original draft, review, and editing. Y.X.W. and X.L.X. provided assistance in material preparation, cell experiments and schematic drawing. Z.X.D., J.L.L. and P.X. helped to establish animal model and assist with CT and MRI. J.L.: Resources and Supervision. Q.J.: Resources. Y.J.F.: Resources and Supervision. X.D.Z.: Resources and project administration. Y.S.: Conceptualization, writing-review and editing, Funding acquisition, and Resources. Z.L.L., M.D.Z., J.Y.Z. and Y.S. prepared the manuscript with inputs from all authors, and all authors contributed to the final review of the manuscript and figures.

Competing interests

The authors declare no competing interests.

Additional information

Supplementary information The online version contains supplementary material available at https://doi.org/10.1038/s41467-025-67035-6.

Correspondence and requests for materials should be addressed to Yong Sun.

Peer review information *Nature Communications* thanks Liming Bian, Yi Cao and the other, anonymous, reviewer(s) for their contribution to the peer review of this work. A peer review file is available.